CHEMISTRY OF MATERIALS

Article

pubs.acs.org/cm

Template-Free Vapor-Phase Growth of Patrónite by Atomic Layer Deposition

Matthew S. Weimer,[†,‡] Robert F. McCarthy,[‡,#] Jonathan D. Emery,[§] Michael J. Bedzyk,[§] Fatih G. Sen,[∥] Alper Kinaci,[∥] Maria K. Y. Chan,[∥] Adam S. Hock,*[,†,⊥] and Alex B. F. Martinson*[,‡]

[†]Department of Chemistry, Illinois Institute of Technology, 3101 South Dearborn Street, Chicago, Illinois 60616, United States

[‡]Materials Science Division, [∥]Center for Nanoscale Materials, and [⊥]Chemical Sciences and Engineering Division, Argonne National Laboratory, 9700 South Cass Avenue, Argonne, Illinois 60439, United States

[§]Department of Materials Science and Engineering, Northwestern University, 2220 Campus Drive, Evanston, Illinois 60208, United States

Supporting Information

ABSTRACT: Despite challenges to control stoichiometry in the vanadium−sulfur system, template-free growth of patrónite, VS_4, thin films is demonstrated for the first time. A novel atomic layer deposition (ALD) process enables the growth of phase pure films and the study of electrical and vibrational properties of the quasi-one-dimensional (1D) transition metal sulfide. Self-limiting surface chemistry during ALD of VS_4 is established via *in situ* quartz crystal microbalance and quadrupole mass spectrometry between 150 and 200 °C. The V precursor, unconventionally, sheds all organic components in the first half-cycle, while the H_2S half-cycle generates the disulfide dimer moiety, S_2^{-2}, and oxidizes V^{3+} to V^{4+}. X-ray analysis establishes VS_4 crystallinity and phase purity, as well as a self-limiting growth rate of 0.33 Å/cy, modest roughness of 2.4 nm, and expected density of 2.7 g/cm^3. Phase pure films enable a new assignment of vibrational modes and corresponding Raman activity of VS_4 that is corroborated by density functional theory (DFT) calculations. Finally, at elevated growth temperatures, a change in the surface mechanism provides a synthetic route to a second vanadium−sulfur phase, V_2S_3.

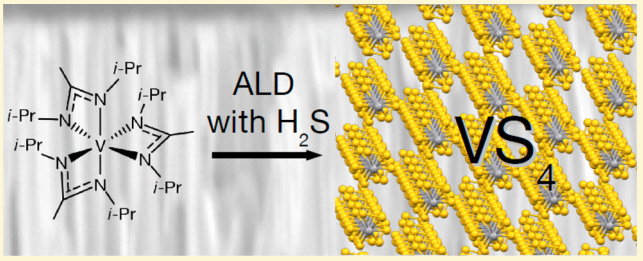

I. INTRODUCTION

The viability and utility of single- and few-atom-layer thick materials have now been firmly established in the wake of graphene's sustained success. This research has led to the exploration and development of semiconducting two-dimensional (2D) materials that exhibit an even more diverse set of optoelectronic properties.[1−3] Transition-metal dichalcogenides (TMDC) have received particular attention due to their layered structure and range of bandgaps.[4−7] Along with a relative ease of synthesis, TMDC and other 2D metal sulfides such as MoS_2,[8−11] WS_2,[12−15] SnS_2,[16−18] NiS,[19,20] and CoS[21,22] have been investigated for various applications, such as electronics, energy storage, energy conversion, and optoelectronics. Most recently, 2D vanadium disulfide, VS_2, has been considered for application in energy storage,[23−25] energy conversion,[26] spintronics,[27] and sensors.[28] Advances in the synthesis of supported[24] and free-standing[26] films of VS_2 have facilitated these new avenues of research.

A subset of transition-metal sulfides possess disulfide (S_2^{-2}) moieties. Recently, facile routes to sulfide minerals based on S_2^{-2} dimers, such as pyrite (FeS_2),[29−31] cattierite (CoS_2),[32,33] and vaesite (NiS_2),[34,35] have been realized, which allows new materials to be integrated in applications such as photovoltaics, catalysis, and energy storage. Patrónite (VS_4) is a lesser-known member of the same transitional metal disulfide class. Patrónite was discovered in 1906,[36] but the structure was not refined until 1964;[37] the cell parameters have only recently been updated.[38] VS_4 can be visualized as being made up of quasi-one-dimensional (1D) chains of $V^{4+}(S_2^{-2})_2$ molecules (Figure 1). Each linear chain is comprised of two S_2^{-2} dimers connecting two adjacent V atoms, with weak van der Waals bonding between 1D chains. This stacked framework provides an interchain distance of 5.83 Å. The 1D structure of VS_4, with a calculated bandgap of 1.0 eV,[39] may provide unique advantages in applications that include Li ion[40,41] and Na ion[42] battery development and supercapacitors,[43] as well as photocatalytic degradation of methylene blue[44] and H_2 generation.[45]

However, controlling vanadium−sulfur stoichiometry has proved synthetically challenging and has thereby hindered progress in these fields. Hydrothermal methods produce pure VS_4 only under specific combinations of synthesis conditions and specific templating substrates.[39] Hydrothermal methods have recently been refined to allow solution dispersed microspheres to be produced template free, but this process

Received: November 29, 2016
Revised: March 9, 2017
Published: March 9, 2017

DOI: 10.1021/acs.chemmater.6b05084
Chem. Mater. 2017, 29, 2864−2873

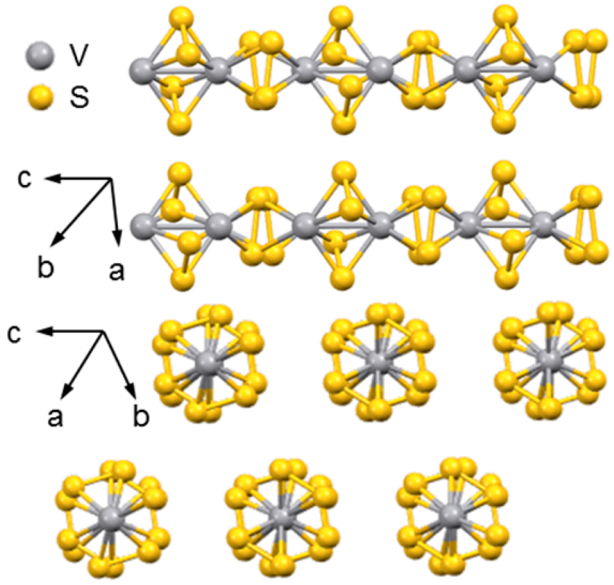

Figure 1. View of the quasi-one-dimensional VS_4 chain (top) and complementary view down the line of VS_4 chains (bottom). Gray balls represent V atoms and yellow balls, S atoms.

requires polymeric coating for the microspheres to remain discrete.[41] Hydrothermal growth of phase-pure films requires a reduced-graphene or reduced-graphene oxide template. Bulk VS_4 has been produced by heating V_2S_3 and S_8[46] or elemental V and S_8 at 400 °C for 3 days to 4 months.[38] In addition to being time-consuming, these methods do not allow for fine thickness control. Finally, VS_4 has been synthesized in organic solvents by combining VCl_4 and hexamethyldisilathiane or hydrogen sulfide (H_2S). However, no continuous thin film growth method has been established through this route.

Atomic layer deposition (ALD) is a vapor-phase deposition technique that relies upon sequential, temporally isolated self-limiting surface chemistry to synthetically modify surfaces one layer at a time. This direct surface synthesis affords the ability to tune materials chemistry through precursor choice as well as enable conformal and pinhole free films over high aspect ratio substrates.[47] While little work has been done on the vanadium/sulfur system, ALD has made significant progress with metal sulfide materials.[48] A relatively recent advance in the tunable chemistry of ALD is the ability to access various metal−sulfur stoichiometries at low temperatures by judicious precursor selection.[49] For example, stoichiometric and phase-pure Cu_2S growth was uniquely achieved only with a Cu(I) precursor but has yet to be produced with a Cu(II) precursor.[50] In addition to phase selectivity via distinct precursor choice, ALD also allows for the same precursor to access different stoichiometric phases at multiple temperature ranges, via different surface chemistry. For example a single Sn precursor may grow hexagonal SnS_2 at 140 °C and orthorhombic SnS above 160 °C.[51]

The relative ease with which vanadium can change between numerous oxidation states makes the isolation of pure VS_4 challenging. This complexity has been recently highlighted in work by Britto et al., in which the nature of the electronic properties resulting from Peierls distorted V−V bonds in the VS_4 crystal structure were only recently clarified.[40] In addition, we are not aware of a theoretical treatment for the origin of the Raman modes visible in the VS_4 spectrum, and the spectrum for VS_2 has only recently been published.[26] While some Raman spectra have been reported for VS_4,[38,42,44] we hypothesize (*vide infra*) that previous spectra include signatures from material with varying degrees of laser damage and oxidation.

Herein, we report template-free thin film growth of VS_4 by ALD up to 200 °C and V_2S_3 from 225 to 250 °C. A self-limiting growth process with alternation of *tris*(*N*,*N*′-diisopropylacetamidinate) vanadium(III) ($V(amd)_3$)[52] and H_2S was observed up to 250 °C, which includes the conformal coating of high aspect-ratio anodic aluminum oxide (AAO) structures. VS_4 films are crystalline as deposited at 200 °C, and V_2S_3 films were crystalline as deposited at 250 °C. Beam damage, to produce V_2O_5, was observed with Raman spectroscopy when using 785 nm laser power above 10% incident power (∼10 mW) for all films grown. However, a pristine VS_4 Raman spectrum was obtained at low laser intensity that we corroborate by density functional theory (DFT) calculations of Raman active modes. Finally, the electronic properties of thin films on insulating substrates reveal finite room temperature conductivity in 1.0 eV bandgap VS_4.

II. METHODS

All atomic layer deposition (ALD) film growth and *in situ* experiments were performed in a commercial hot-wall ALD tool (Savannah 200, Cambridge NanoTech) modified for H_2S compatibility.[53] A constant 10 sccm stream of ultrahigh purity nitrogen carrier/purge gas, purified with an Entegris Gatekeeper metal purifier to ensure H_2O and O_2 levels were <250 ppt, was continuously pumped through the tool resulting in a base pressure of 0.4 Torr. *tris*(*N*,*N*′-Diisopropylacetamidinate) vanadium(III) ($V(amd)_3$) was synthesized and purified according to published procedures.[52] $V(amd)_3$ was delivered under its own vapor pressure (without bubbling or nitrogen assistance) from a 50 cm^3 stainless steel cylinder heated to 190 °C. A dilute hydrogen sulfide (H_2S) mixture (4% in N_2, Airgas) was stepped down to 500 Torr relative to vacuum through a two-stage regulator before further reducing the flow through a 300 μm pinhole just prior to the pneumatic ALD valve. The precursor pulsing sequence follows the format $t_1-t_2-t_3-t_4$, where t_1 is the $V(amd)_3$ pulse time; t_3 is the H_2S pulse time; t_2 and t_4 are the purge times following the $V(amd)_3$ and H_2S pulses, respectively. Times are reported in seconds.

Quartz crystal microbalance (QCM) measurements were performed with a modified reactor lid wherein mass changes may be monitored *in situ* directly adjacent to and simultaneous to *ex situ* film growth as previously described.[54] The lid has two QCMs collinear with the reactor inlet and outlet. The "Front QCM" is positioned two inches downstream from the inlet, and the "Back QCM" lies six inches farther downstream.

Quadrupole mass spectrometry (QMS) measurements were performed *in situ* using an RGA200 (Stanford Research Systems) whereby residual precursor and reaction byproduct gases were differentially pumped through a 35 μm orifice that samples reaction chamber exhaust. An electron multiplier (1000× gain) increased sensitivity, and data acquisition occurred through the RGA Windows software package standard with the system. Exhaust lines were kept at 120 °C to minimize condensation of gas phase species prior to reaching the quadrupole.

Films for *ex situ* analysis were deposited on Si(100) substrates with native oxide, fused quartz, and anodic aluminum oxide (AAO) membranes. Films were grown within three inches of the inlet. Prior to growth, flat substrates, fused quartz, and native oxide Si were subjected to 10 min of acetone sonication, a rinse, 10 min of isopropanol sonication, a rinse, a N_2 blast dry, and a minimum 60 min of in-tool thermal equilibration time. AAO disks were Whatman Anodisk 13 (#6809-7023), 13 mm in diameter, with 200 nm channels and a 20 nm pore opening at one end with a 50 μm disk thickness (250:1 aspect ratio when coated from the 200 nm opening). AAOs were subjected to 2 min of DI water sonication, followed by sonication in acetone and isopropanol for 2 min each, and a final DI rinse. AAOs were dried

DOI: 10.1021/acs.chemmater.6b05084
Chem. Mater. 2017, 29, 2864−2873

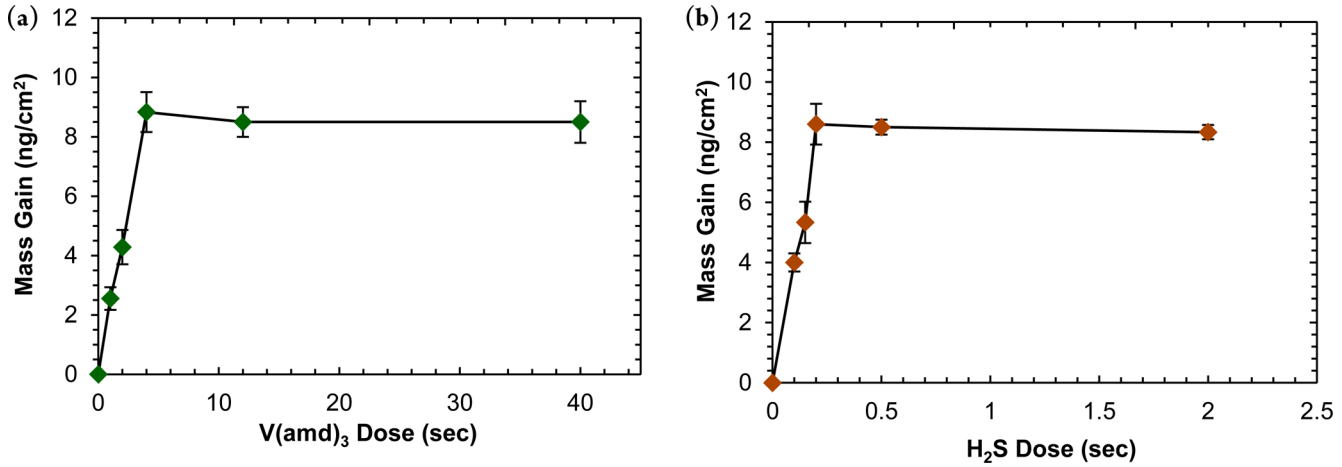

Figure 2. Dose and purge QCM data taken at 200 °C for the $V(amd)_3/H_2S$ process. Dose sequence for (a) is x−30 s−0.5 s−30 s, where x is the dose time for $V(amd)_3$. 12 s doses were achieved with three, 4 s pulses and 40 s was achieved with five, 8 s pulses; each dose was separated by 30 s purge time to build vapor pressure of $V(amd)_3$. Dose sequence for (b) is 6 s−30 s−x−30 s, where x is the dose time for H_2S. Lines are added to the plots to aid the eye.

under reduced pressure and spent a minimum of 60 min in the tool for temperature equilibration prior to growth. All films used the growth sequence optimized from saturation studies: 6 s (consisting of three, 2 s doses separated by 30 s purge to build $V(amd)_3$ vapor pressure) $V(amd)_3$ dose, 30 s purge, 0.5 s H_2S dose, and 30 s purge.

The crystallinity and crystalline orientation of VS_x films on fused quartz and AAO were determined by X-ray diffraction (XRD). XRD measurements were acquired with a Bruker Advance D8 Powder X-ray Diffractometer with Ni-filtered Cu Kα radiation (wavelength λ = 1.540 Å) operating at 40 kV and 40 mA. The scan range was between 10° and 80° with 0.01° steps at a collection speed of 0.75 to 3 s/step depending on film thickness. Film thickness, density, and roughness were determined by X-ray reflectivity (XRR, Philips X'Pert Pro MRD diffractometer, Cu Kα radiation). XRR data were foot-print corrected and fit using the Abeles matrix method within the Motofit software package.[55] XRR fits were limited at $q = 4\pi \sin(\theta)/\lambda$ = ∼0.04 and 0.15 $Å^{-1}$, where θ is the incident beam angle. Errors on XRR fit parameters were estimated to be within 95% confidence level using χ^2 mapping.

Surface Raman spectroscopic measurements of films were taken with an Innovative Photonics Solutions 100 mW 785 nm laser (model #I0785SR0100B) in a Renishaw spectrophotometer in backscattering configuration, using a Renishaw CCD camera, a 100 cm^{-1} edge filter, and a 1200 l/mm diffraction grating allowing for a resolution of ∼2 cm^{-1}. The system was calibrated to the Si peak (520 cm^{-1}) before measurements. Care was taken to avoid beam damage and subsequent oxidation to the films by maintaining low laser intensity (below 10% of 100 mW) during measurements and performing visual inspection with a 50× magnification microscope lens after each measurement.

Resistivity and mobility measurements were acquired with a Hall measurement system (HMS-3000, Ecopia) at room temperature. Samples were measured in a N_2 atmosphere glovebox with a 0.57 T magnet prior to air exposure as well as in ambient conditions with a 0.55 T magnet. No difference was observed between measurements under inert atmosphere and in ambient conditions.

Thickness and composition were corroborated by scanning electron microscopy (SEM) on a Phenom ProX equipped with an energy dispersive X-ray spectroscopy (EDX) detector for elemental analysis. SEM and EDX measurements were taken with a high-vacuum sample holder, and samples were attached to the removable SEM stage by carbon tape. SEM measurements were taken 2 mm below the sample holder horizon, while EDX measurements were taken 3 mm below the sample holder horizon.

XPS data were acquired using a Thermo Scientific ESCALAB 250Xi equipped with monochromated, microfocused (900 μm spot size) Al Kα X-rays and a 180° double-focusing hemispherical analyzer. Samples were ion-beam etched for 30 s using 3 keV Ar^+ ions to remove ∼10 nm of adventitious carbon and surface oxides. All data were calibrated to the C 1s signal.

First-principles density functional theory (DFT) calculations[56] were employed to predict the nonresonant first-order VS_4 Raman spectrum. The VS_4 unit cell[37] was fully relaxed using the plane-wave DFT code Vienna Ab initio Simulation Package (VASP).[57,58] Projector augmented wave (PAW) potentials were used for vanadium and sulfur. These potentials include five and six valence electrons for V and S, respectively. The Perdew-Burke-Ernzerhof (PBE)[59] parametrization of the generalized gradient approximation (GGA) was employed for electronic exchange correlation. The kinetic energy cutoff for plane waves was selected as 520 eV.

The Raman scattering activity of a Brillouin zone center phonon is related to the change in dielectric tensor upon excitation of that phonon. To obtain Raman activities, we followed the method[60] detailed in the Supporting Information. This framework was implemented in a *Python* script by Fornari and Stauffer.[61]

After unit cell optimization, the dynamical matrix was calculated for VS_4 using VASP. Then, each phonon mode at the Brillouin zone center was excited by displacing the atoms along the corresponding phonon eigenvector. The change in dielectric tensor from such displacements was computed by density functional perturbation theory and, accordingly, Raman activity was obtained.

III. RESULTS AND DISCUSSION

The vanadium−sulfur phase space remains largely unexplored in atomic layer deposition (ALD). Only one example exists; the *tris*(*N*,*N*′-diisopropylacetamidinate) vanadium(III) ($V(amd)_3$) and hydrogen sulfide (H_2S) process has been utilized as a minority dopant in a β-In_2S_3 bulk film.[52] V^{3+} substitution into In^{3+} lattice positions up to 25%, by atomic ratio, is achieved when the In_2S_3 ALD process is replaced by the $V(amd)_3/H_2S$ process during growth of the intermediate band material, $V_xIn_{2-x}S_3$. While the $V(amd)_3/H_2S$ process showed self-limiting behavior when substituted for a single cycle of the In_2S_3 process, no full saturation study had been performed. Figure 2 shows saturative dose behavior for each precursor at 200 °C when measured by *in situ* quartz crystal microbalance (QCM). From these data, we see that a 4 s dose of $V(amd)_3$ and 0.2 s dose of H_2S are sufficient dose lengths for self-saturation. Due to the low volatility of $V(amd)_3$ and the temperature limitations of the Savannah 200 ALD reactor, long $V(amd)_3$ pulses were comprised of a set of shorter pulses separated by 30 s of purge time to build vapor pressure. This

DOI: 10.1021/acs.chemmater.6b05084
Chem. Mater. 2017, 29, 2864−2873

process ensured that the number of moles of $V(amd)_3$ introduced over long doses was equivalent to shorter doses. Purge length studies (Figure S1) show that a 30 s purge time is sufficient to avoid uncontrolled growth via reaction of physisorbed precursors.

To investigate the effect of temperature on the growth rate, *in situ* QCM and *ex situ* X-ray reflectivity (XRR) experiments were performed. Figure 3 shows the mass gain as a function of

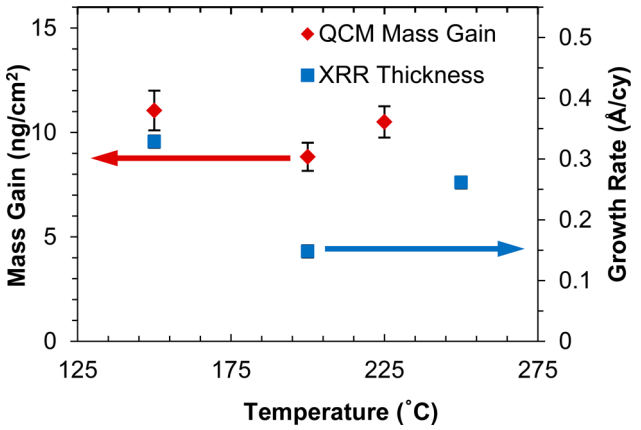

Figure 3. Mass gain *in situ* QCM data for the $V(amd)_3/H_2S$ process (red diamond) with corresponding growth rates as measured by XRR (blue square) for films grown on native oxide Si(100).

temperature as measured by *in situ* QCM (red diamonds) from 150 to 225 °C and the corresponding growth rates as measured with XRR (blue squares) from 150 to 250 °C on native oxide Si. Limitations inherent in the quartz crystal due to temperature sensitivity restrict the functional limit for this QCM setup to 225 °C. Self-limiting behavior was observed from 150 to 225 °C, as evidenced by QCM dose studies of each precursor at 150, 200, and 225 °C. An example of dose saturation studies performed at 200 °C is shown in Figure 2. As was the case at 200 °C, both of the other temperatures showed that a 4 s $V(amd)_3$ dose was necessary for saturation. The mass gain measured by QCM decreased from 11.1 ± 0.9 ng/cm^2 at 150 °C, corresponding to a growth rate of 0.33 ± 0.01 Å/cy by XRR, to 8.8 ± 0.7 ng/cm^2 (0.15 ± 0.01 Å/cy) at 200 °C, as qualitatively expected. However, a slight increase in growth rate to 10.5 ± 0.01 Å/cy (0.26 ± 0.01 Å/cy) at 250 °C is not normal for ALD of sulfides. For ALD of metal sulfides, mass gain and growth rate tend to decrease with increasing temperature, mirroring the equilibrium density of surface −SH species, as first noted in growth of GaS_x by ALD.[62] The mechanism for this temperature dependence has been hypothesized to result from the conversion of neighboring surface sulfhydryl species (−SH) into a bridging sulfur surface species (−S−) with evolution of gaseous H_2S (Scheme 1).[63] The increase in growth rate at 250 °C suggests a deviation perhaps due to the earliest stage onset of nonself-limiting deposition/decomposition. Alternatively, this increase in

Scheme 1. Conversion of Surface Sulfhydryl Species to Bridging Surface Sulfur and Gaseous H_2S

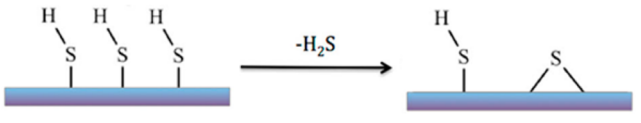

growth rate could signal the accessibility of a different surface chemistry, which may lead to different film composition (stoichiometry). QCM $V(amd)_3$ dose studies at a lower, 225 °C, growth temperature demonstrate that decomposition or uncontrolled growth does not occur, as introducing more $V(amd)_3$ after a 4 s saturative dose did not increase the mass gain per cycle. This suggests that films grown at temperatures of 225 °C or greater may have a V−S composition different from films grown below 200 °C as will be examined in detail *vide infra*.

The growth rate per cycle was constant over long depositions, and no nucleation delay was noted by QCM on a fresh ALD Al_2O_3 surface (Figure S2). Figure 4 shows a

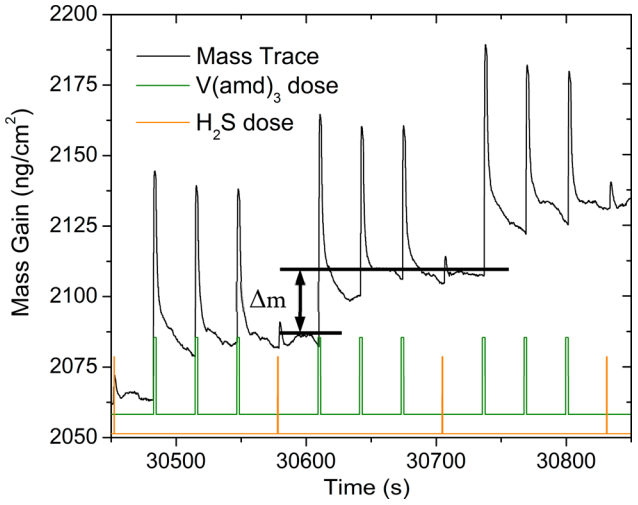

Figure 4. *In situ* QCM mass gain data for the $V(amd)_3/H_2S$ process at 200 °C (black, top) with corresponding binary dose traces for $V(amd)_3$ (green, middle) and H_2S (orange, bottom).

zoomed portion of a 1500 cy deposition at 200 °C. From the mass trace (black), we see a significant mass gain (Δm) of 8.8 ± 0.7 ng/cm^2/cycle associated with the $V(amd)_3$ pulses (green). The spike at the beginning of each $V(amd)_3$ dose is a convolution of dose-induced changes in reactor pressure and surface temperature, to which the quartz crystal oscillations are also sensitive, in addition to potential physisorption and rapid desorption of $V(amd)_3$ precursor on the crystal surface. Interestingly, no mass change was observed during the H_2S pulse (orange). Normally, in the case of large amidinate ligands (m = 142), an overall mass loss is observed during the nonmetal dose which corresponds to the loss of organic ligands and generation of the less massive surface sulfhydryl species (m = 33).[47] Thus, to maintain constant mass, ∼4.3 sulfhydryl groups replace each remaining amidinate ligand, or we convert bridging sulfur bonds to sulfhydryl with nominal mass gain from the added hydrogen.

Corresponding quadrupole mass spectrometry (QMS) measurements revealed fragments corresponding to the protonated ligand (H−amd) and unreacted precursor during the $V(amd)_3$ pulse. However, no H−amd is observed during the H_2S pulse at 150 or 200 °C (Figure S4). While full removal of all ligands during the metal half-cycle is not common, surface metal surface species devoid of ligands may be unreactive to further gas-phase metal-containing precursor, producing self-limiting behavior. From the above *in situ* QCM and this QMS

DOI: 10.1021/acs.chemmater.6b05084
Chem. Mater. 2017, 29, 2864−2873

data, we present one hypothetical mechanism that is consistent with these data, eqs 1 and 2:

$$(-SH)_3^* + V(amd)_3 \rightarrow (-S)_3V^* + 3[H(amd)] \quad (1)$$

$$2(-S)_3V^* + xH_2S \rightarrow 2(-S)_{3-x}V(SH)_x^* \quad (2)$$

where the asterisk (*) denotes a surface species. In eq 1, all of the amidinate ligands are lost from reaction with surface sulfhydryl species. Thus, the H_2S half-cycle exists to repopulate the surface with sulfhydryl groups. However, the mechanism of repopulation is not obvious. We speculate that the process may occur through proton transfer from a S−H bond to a bridging sulfide group, the reverse of Scheme 1. This mechanism would maintain the oxidation state of vanadium and produce V_2S_3 films. Alternatively, generation of two sulfanyl radicals ($SH^\bullet$) could lead to oxidation of surface vanadium species as well as generation of new disulfide dimers ($(S-S)^{2-}$) and S−H moieties around the metal. This process would likely also generate hydrogen molecules (H_2). Metal sulfides are known to undergo sulfurization in the presence of H_2S which generates H_2 and oxidizes the metal.[64] Further experiments are required to more fully determine the mechanism of the H_2S half-reaction.

In order to better understand the nature of synthesized films, and thereby the surface chemistries proposed from QCM and QMS data, *ex situ* characterization of films grown on native oxide Si(100), quartz, and AAO substrates at 150, 200, and 250 °C were performed. Figure 5 shows XRR data for films grown

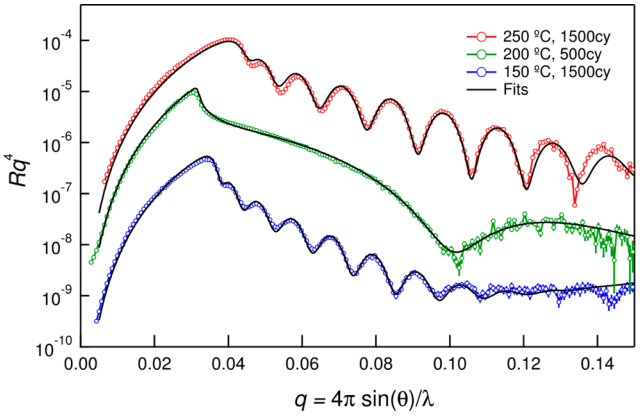

Figure 5. X-ray reflectivity data and fits (black lines) for VS_4 and V_2S_3 films grown on native oxide Si of 1500 cy at 150 °C (blue), 500 cy at 200 °C (green), and 1500 cy at 250 °C (red).

at 150 °C (1500 cy), 200 °C (500 cy), and 250 °C (1500 cy) on native oxide-Si (100) and the corresponding modeled fits. Fitted parameters for these data are tabulated in Table 1. The growth rate trends are in general agreement with QCM results and provide further information about film density and roughness. Film roughnesses are approximately constant at 2 nm roughness regardless of growth temperature and thickness. The density, however, shows clear contrast between the 200 and 250 °C data. Films grown at 150 and 200 °C exhibit a density (2.8 ± 0.1 g/cm^3) in agreement with the expected value for a nearly fully dense VS_4 film (2.8 g/cm^3). In contrast, the 250 °C growth is approximately 50% denser (4.2 g/cm^3) than both the 150 and 200 °C film. This density is much closer to that expected for a V_2S_3 film (4.7 g/cm^3). While the XRR-derived densities are ∼10% less than that expected for a fully dense V_2S_3 film, this is common for polycrystalline thin films grown by ALD.[49] Persistent VS_4 inclusions within the films grown at 250 °C cannot, however, be ruled out by density alone and require further characterization.

Table 1. XRR-Derived t (Thickness), σ (Roughness), and ρ (Density) Values Acquired from Fits Presented in Figure 5[a]

T (°C)	χ^2	t (nm)	σ (nm)	ρ (g/cm^3)
150	1.98	$49.3^{+0.6}_{-0.6}$	$2.4^{+0.2}_{-0.1}$	$2.9^{+0.1}_{-0.2}$
200	4.76	$7.4^{+0.5}_{-0.5}$	$1.9^{+0.3}_{-0.1}$	$2.7^{+0.1}_{-0.2}$
250	7.52	$39.2^{+0.2}_{-0.4}$	$1.7^{+0.1}_{-0.2}$	$4.2^{+0.1}_{-0.2}$

[a]Goodness-of fit parameter $\chi^2 = (N - N_p)^{-1}\sum_k((I_{meas,k} - I_{calc,k})^2/Err_k^2)$, where $I_{meas,k}$ and $I_{calc,k}$ are the measured and calculated intensities of the k^{th} data point, respectively. Err_k is the uncertainty for the data point, and N and N_p represent the total number of data points and fitting parameters. Error bounds define the 95% confidence interval for each parameter.

The crystalline nature of films grown at different temperatures on anodic aluminum oxide disks (AAOs) was investigated with X-ray diffraction (XRD) (Figure 6). These measurements show that films grown at 150 °C were

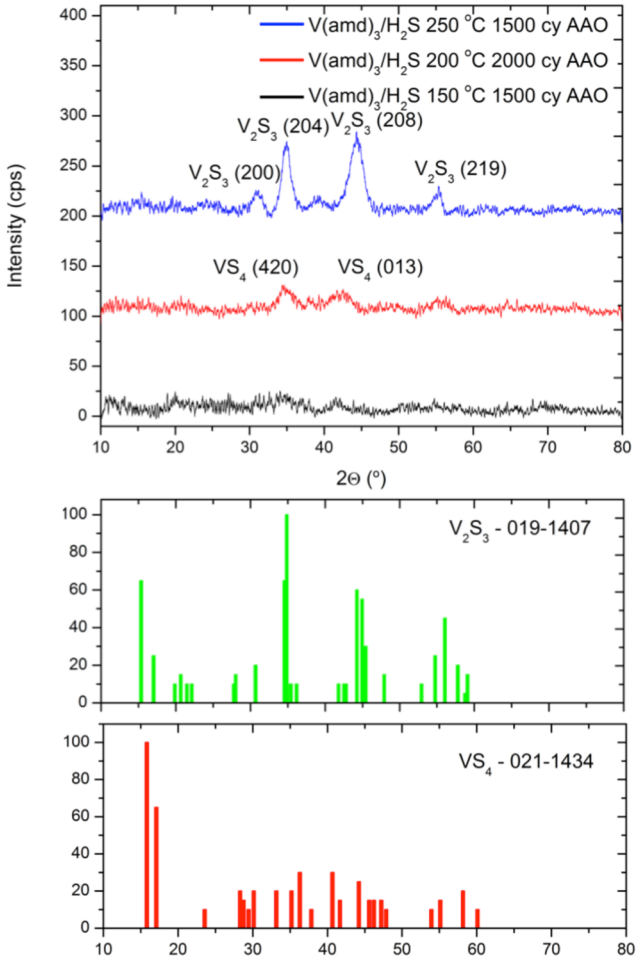

Figure 6. X-ray diffraction (XRD) from the $V(amd)_3/H_2S$ process grown on anodic aluminum oxide (AAO) disks. Traces have been offset for clarity. The thicknesses for these films are as follows: 150 °C, 49.3 nm; 200 °C, ∼22.2 nm; 250 °C, 39.2 nm. Reference spectra for V_2S_3 (green, middle) and VS_4 (red, bottom) are provided for comparison.

DOI: 10.1021/acs.chemmater.6b05084
Chem. Mater. 2017, 29, 2864−2873

amorphous or very weakly crystalline. However, films grown at 200 °C exhibit two broad crystalline diffraction peaks. These features are difficult to uniquely index due to the breadth of the full-width at half-maximum and the possibilities of overlapping peaks from other vanadium−sulfur phases. However, the (420) and (013) peaks of VS_4 (JCPDS 021-1434)[65] fall within this range. Films grown at 250 °C have sharper features that can be indexed to V_2S_3 (JCPDS 019-1407).[66] The XRD peak assignments are further supported by the modeled XRR density of the films *vide supra*.

To further corroborate the phase assignment, Raman spectroscopy was also performed for films on fused quartz. Films exposed to a 785 nm, 100 mW laser above 10% intensity were found to be susceptible to beam damage, creating V_2O_5 (Figures S5 and S6). As such, care was taken to ensure all spectra included here are from undamaged samples. Figure 7

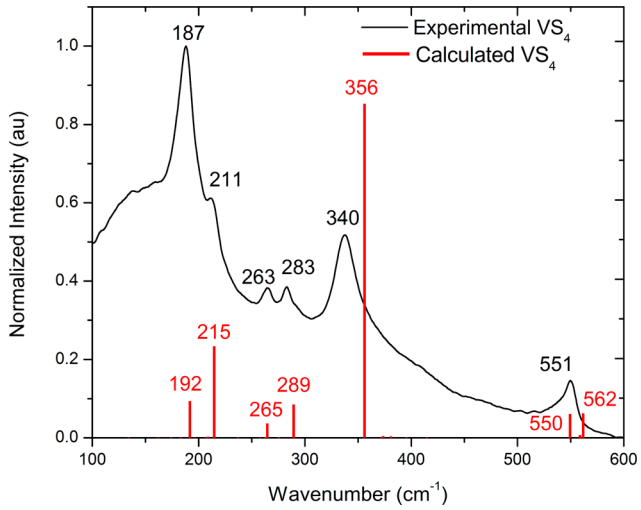

Figure 7. Raman spectroscopy for VS_4 film grown at 200 °C, ∼22.2 nm thick, on fused quartz (black line). DFT calculated frequencies are overlaid (red bar) for clarity. The broad peak from ∼100 to 225 cm^{-1} is from the quartz substrate.

shows Raman spectroscopic data for a 1500 cycle film of the $V(amd)_3/H_2S$ process grown at 200 °C (black line). When compared with known vanadium sulfide species, V_3S_4,[67] VS_2,[26] and VS_4,[38,42,44] no obvious match is found. However, we further examine the validity of literature references and the RRUFF database (ID R070737) spectra for VS_4 (http://rruff.info/patronite/display=default/). Close inspection reveals that the RRUFF database spectra acquired with 532 nm (ca. 2.33 eV) laser at 40% intensity (of 150 mW) and a reference V_2O_5 spectrum are identical (Figure S7). However, the spectrum taken with the 780 nm laser (ca. 1.59 eV) and 40% intensity (of 600 mW) appears to be a mixture of V_2O_5 and a different, unidentified material. The two most prominent features from our experimental spectrum, taken at 785 nm (1.58 eV) and 10% intensity (of 100 mW), are observed at 187 and 340 cm^{-1}. The V_2O_5 Raman spectrum has a strong peak at 140 cm^{-1} and a mixture of the B_{1g} and B_{3g} modes and reflects the long-range order of the in plane V−O layers.[68] Neither the RRUFF spectrum taken at 532 nm laser nor the V_2O_5 Raman spectra have a feature at 340 cm^{-1}. Additionally, our experimental spectrum does not have any features above ca. 551 cm^{-1} (Figure S7), while both the RRUFF 780 and 532 nm spectra have features at 995 cm^{-1}. Thus, neither RRUFF spectrum can be considered pure VS_4.

To clarify the ambiguities in the available Raman spectroscopic data in the literature, we determined the Raman spectrum of patrónite, VS_4, using DFT calculations. The Raman active phonon modes and their corresponding normalized intensities are given in Figure 7 (red bars). We identified seven Raman active modes for the VS_4 patrónite structure. The modes at 192 and 215 cm^{-1} are attributed to V−S bond stretching. The mode at 356 cm^{-1} is a breathing mode of the V_2S_4-cages. The modes at 265, 289, 550, and 562 cm^{-1} are identified as S−S bond stretching/twisting. Atomic structures and animations of phonon modes are given in the Supporting Information. Figure 7 shows the overlay plot of these computational results with experimental results, which are in good agreement, with a mean absolute percentage error of 2% and a standard deviation in absolute percentage error of 1%. The 340 cm^{-1} peak shows the largest error at 16 wavenumbers or 4.7%.

No vibrational modes above 565 cm^{-1} were found from the calculated spectrum, providing further evidence that the spectra provided in the RRUFF database correspond to samples that have beam damage. We have also computed the phonon spectra of monoclinic VO_2, which like VS_4, contains bonds between V^{4+} and −2 anions (O^{2-} vs S_2^{2-}). The highest frequency for VO_2 was 667 cm^{-1}. Thus, it seems physically unlikely that a 995 cm^{-1} mode corresponds to VS_4.

Films grown at 150 °C had a similar Raman spectrum; however, films grown at 250 °C became Raman silent as expected for V_2S_3 (Figure S8). No signs of other vanadium−sulfur species were observed in Raman spectra for films grown at 250 °C. These films were much less susceptible to beam damage at 785 nm and 100% intensity of 100 mW and appeared stable for minutes under these conditions. From the XRR, XRD, and Raman spectroscopy experiments, as well as DFT calculations, it appears that films grown at 150 to 200 °C can be assigned to VS_4 while crystalline V_2S_3 starts to grow by a different mechanism before 250 °C but after 200 °C.

XPS was performed on two sets of samples grown at 150, 200, 250 °C on native oxide Si and fused quartz (Figure S16); no difference was noted between substrates. The spectra are dominated by V and S photoelectron and Auger signals and show no observable difference in elemental composition between temperatures. In addition to V and S signals, weak O, N, and C signals are present in the survey spectra. High-resolution scans (0.05 eV steps) of two spectral regions were performed (Figure S17). For all specimens, the separation between peaks of the V doublet is Δ_V = 7.6 eV; the peak V $2p_{3/2}$ and V $2p_{1/2}$ positions are near 513 and 520 eV, respectively, and the peak shapes are asymmetric. These data suggest that the V present within the films is metallic as opposed to an expected V_xS_y species. However, reduction of transition metal oxides and sulfides under Ar^+ bombardment is well-documented.[69−71] The high probability of reduction makes chemical analysis through XPS inconclusive. However, a small (∼1 eV) and systematic shift to higher binding energy observed with a decrease in deposition temperature suggests an increase in oxidation state for the 150 and 200 °C grown films. This is consistent with both Raman spectroscopic and X-ray diffraction data which identifies films grown at 150 and 200 °C to be V^{4+} and 250 °C to be V^{3+}.

The binding energy of the S $2p_{3/2}$ signal in all three films is centered near 162 eV (Figure S17), in line with literature values

DOI: 10.1021/acs.chemmater.6b05084
Chem. Mater. 2017, 29, 2864−2873

for metal-sulfide binding energies.[39] In the S 2p signal, we observe a small (~0.5 eV) and systematic shift to lower binding energies in films grown at lower temperatures, which may indicate a difference in oxidation state. However, it is difficult to conclude chemical state from this data due to the unknown bonding configuration of S after Ar^+ ion reduction of the V_xS_y compounds. Further, literature values report that the binding energy of S $2p_{3/2}$ for both V_2S_3 and VS_4 fall between 162 and 163 eV,[72,73] making tenuous any conclusions derived from the apparent shift in the S 2p data. Finally, the S/V integrated peak intensity ratios are approximately equivalent for films grown at 150 and 200 °C (3.35 and 3.47, respectively, 4 expected for VS_4), while the ratio for the film grown at 250 °C is 2.99 (1.5 expected for V_2S_3). While these numbers are not in agreement with expected values, the rate of sputtering is known to be greater for S than transition metals.[74] Notwithstanding different sputtering rates, the increased relative concentration of V in the 250 °C film is consistent with a larger phase fraction of V_2S_3 within those films.

In light of these conclusions, we hypothesize the H_2S half-cycle surface reaction mechanism to follow two distinct pathways. Until 200 °C, an oxidative mechanism occurs which generates S−S bonds and thus disulfide dimer moieties, S_2^{-2}, as shown in eq 3:

$$(-S)_3V^* + xH_2S \rightarrow (-S)_{4-2x}V(SSH)_x^* + \frac{1}{2}xH_2 \quad (3)$$

where the asterisk (*) denotes a surface species. From this process, V is also oxidized from 3+ to 4+ and H_2 is produced. Alternately, S_2^{-2} and V oxidation could occur through a series of radical-induced transformations. Either mechanism would grow VS_4. No H_2 was observed in QMS data during the H_2S pulse, suggesting radical surface chemistry; however, more detailed studies would be required to confirm a mechanism. Above 200 °C, the surface chemistry may follow eq 2, in which repopulation of the surface sulfhydryl species occurs without a change in precursor oxidation states (formally V^{3+} and S^{-1}), resulting in growth of V_2S_3. It is unlikely that V_2S_3 is formed via decomposition of VS_4 above 200 °C, as VS_4 has previously been shown to be stable up to 400 °C.[75] Furthermore, VS_4 can be synthesized from V_2S_3 and S_8 at 400 °C.[46]

Scanning electron microscopy (SEM) was performed on AAO disks (aspect ratio of ca. 250:1) coated with ~22.2 nm of VS_4 at 200 °C. (Figure S18) It can be seen that this middle portion of the channel is coated without voids. Additionally, no pinching occurs at the open end (200 nm wide channel) of the disk as a result of the VS_4 growth. Vanadium can be seen throughout the length of the channel by EDX (Figure S19). The small end of the channel is closed, as expected given the amount of VS_4 grown (22.2 nm) is much greater than half the diameter of the small opening (ca. 10 nm).

Finally, bulk electrical properties of VS_4 and V_2S_3 films were investigated with Hall measurements, tabulated in the Supporting Information, which show a growth temperature dependence on the resistivity and mobility of films grown from 150 to 250 °C. The resistivity of VS_4 films decreases between growth temperatures of 150 and 200 °C, 3.63×10^{-4} to 3.83×10^{-5} Ω cm, with a corresponding increase in mobility, 5.65×10^{-2} to 1.48×10^{-1} $cm^2/(V\ s)$. A second difference between VS_4 and V_2S_3 is shown by an increase in resistivity, from 3.83×10^{-5} to 3.19×10^{-4} Ω cm, while mobility remains approximately constant, 1.48×10^{-1} to 1.54×10^{-1} $cm^2/(V\ s)$, for films grown at 200 and 250 °C.

IV. CONCLUSION

Patrónite, VS_4, thin films were grown for the first time without a structure−directing template. Self-limiting surface reactions of the *tris*(*N*,*N*′-diisopropylacetamidinate) vanadium(III) (V-(amd)$_3$) and H_2S process were observed to produce dense, polycrystalline V_2S_3 films at temperatures above 225 °C, while lower temperature deposition results in amorphous or weakly crystalline VS_4. *In situ* studies suggest that nearly all amidinate ligands are lost in the V(amd)$_3$ half-cycle, which complicates the determination of H_2S half-cycle surface chemistry. The first non-beam-damaged VS_4 Raman spectrum was acquired and corroborated with DFT calculations. The novel low temperature ALD process adds two new metal sulfide phases to the list of ALD-accessible materials.

■ ASSOCIATED CONTENT

Supporting Information

The Supporting Information is available free of charge on the ACS Publications website at DOI: 10.1021/acs.chemmater.6b05084.

Varying purge length data for QCM saturation studies, QCM data for 1500 cycles of the V(amd)$_3$/H_2S, QMS data for the V(amd)$_3$/H_2S process at 150 and 200 °C, Raman spectroscopic data showing beam damage on films grown at 200 °C, RRUFF VS_4 reference Raman spectra, V_2O_5 Raman spectra, VS_4 Raman spectrum from 1100 to 100 cm^{-1}, Raman spectrum for films grown at 250 °C, details for Raman activity intensity calculations, tabulated calculated VS_4 Raman modes, visualizations of select DFT-calculated Raman modes, tabulated values for Hall measurements, and EDX data for VS_4 films (PDF)
Computed vibrational mode #40 (AVI)
Computed vibrational mode #33 (AVI)
Computed vibrational mode #26 (AVI)
Computed vibrational mode #21 (AVI)
Computed vibrational mode #20 (AVI)
Computed vibrational mode #7 (AVI)
Computed vibrational mode #1 (AVI)

■ AUTHOR INFORMATION

Corresponding Authors

*E-mail: ahock@iit.edu (A.S.H.).
*E-mail: martinson@anl.gov (A.B.F.M.).

ORCID

Matthew S. Weimer: 0000-0002-5969-6415
Michael J. Bedzyk: 0000-0002-1026-4558
Maria K. Y. Chan: 0000-0003-0922-1363
Adam S. Hock: 0000-0003-1440-1473
Alex B. F. Martinson: 0000-0003-3916-1672

Present Address

#R.F.M.: Microlink Devices, Inc., 6457 West Howard Street, Niles, Illinois, 60714.

Author Contributions

All authors have given approval to the final version of the manuscript.

Notes

The authors declare no competing financial interest.

DOI: 10.1021/acs.chemmater.6b05084
Chem. Mater. 2017, 29, 2864−2873

■ ACKNOWLEDGMENTS

Work at Argonne National Laboratory was supported under U.S. Department of Energy Contract DE-AC02-06CH11357. M.S.W. acknowledges support from the ARCS foundation and the IIT Department of Chemistry Kilpatrick Fellowship. A.S.H. thanks the Illinois Institute of Technology for funding and start-up support. Work by M.J.B. and A.B.F.M was supported by Argonne-Northwestern Solar Energy Research (ANSER) Center, an Energy Frontier Research Center funded by DOE, Office of Science, BES under Award # DE-SC0001059. Work by J.D.E. was supported by the Northwestern Argonne Institute of Science and Engineering (NAISE). This work was performed, in part, at the Center for Nanoscale Materials, a U.S. Department of Energy Office of Science User Facility under Contract No. DE-AC02-06CH11357.

■ REFERENCES

(1) Butler, S. Z.; Hollen, S. M.; Cao, L.; Cui, Y.; Gupta, J. A.; Gutiérrez, H. R.; Heinz, T. F.; Hong, S. S.; Huang, J.; Ismach, A. F.; Johnston-Halperin, E.; Kuno, M.; Plashnitsa, V. V.; Robinson, R. D.; Ruoff, R. S.; Salahuddin, S.; Shan, J.; Shi, L.; Spencer, M. G.; Terrones, M.; Windl, W.; Goldberger, J. E. Progress, Challenges, and Opportunities in Two-Dimensional Materials Beyond Graphene. *ACS Nano* **2013**, *7*, 2898−2926.

(2) Das, S.; Robinson, J. A.; Dubey, M.; Terrones, H.; Terrones, M. Beyond Graphene: Progress in Novel Two-Dimensional Materials and van der Waals Solids. *Annu. Rev. Mater. Res.* **2015**, *45*, 1−27.

(3) Bhimanapati, G. R.; Lin, Z.; Meunier, V.; Jung, Y.; Cha, J.; Das, S.; Xiao, D.; Son, Y.; Strano, M. S.; Cooper, V. R.; Liang, L.; Louie, S. G.; Ringe, E.; Zhou, W.; Kim, S. S.; Naik, R. R.; Sumpter, B. G.; Terrones, H.; Xia, F.; Wang, Y.; Zhu, J.; Akinwande, D.; Alem, N.; Schuller, J. A.; Schaak, R. E.; Terrones, M.; Robinson, J. A. Recent Advances in Two-Dimensional Materials beyond Graphene. *ACS Nano* **2015**, *9*, 11509−11539.

(4) Eda, G.; Yamaguchi, H.; Voiry, D.; Fujita, T.; Chen, M.; Chhowalla, M. Photoluminescence from Chemically Exfoliated MoS_2. *Nano Lett.* **2011**, *11*, 5111−5116.

(5) Cao, T.; Wang, G.; Han, W.; Ye, H.; Zhu, C.; Shi, J.; Niu, Q.; Tan, P.; Wang, E.; Liu, B.; Feng, J. Valley-selective circular dichroism of monolayer molybdenum disulphide. *Nat. Commun.* **2012**, *3*, 887.

(6) Wang, Q. H.; Kalantar-Zadeh, K.; Kis, A.; Coleman, J. N.; Strano, M. S. Electronics and optoelectronics of two-dimensional transition metal dichalcogenides. *Nat. Nanotechnol.* **2012**, *7*, 699−712.

(7) Johari, P.; Shenoy, V. B. Tuning the Electronic Properties of Semiconducting Transition Metal Dichalcogenides by Applying Mechanical Strains. *ACS Nano* **2012**, *6*, 5449−5456.

(8) Rao, C. N. R.; Maitra, U.; Waghmare, U. V. Extraordinary attributes of 2-dimensional MoS_2 nanosheets. *Chem. Phys. Lett.* **2014**, *609*, 172−183.

(9) Jaramillo, T. F.; Jørgensen, K. P.; Bonde, J.; Nielsen, J. H.; Horch, S.; Chorkendorff, I. Identification of Active Edge Sites for Electrochemical H_2 Evolution from MoS_2 Nanocatalysts. *Science* **2007**, *317*, 100−102.

(10) Splendiani, A.; Sun, L.; Zhang, Y.; Li, T.; Kim, J.; Chim, C.-Y.; Galli, G.; Wang, F. Emerging Photoluminescence in Monolayer MoS_2. *Nano Lett.* **2010**, *10*, 1271−1275.

(11) Yang, Y.; Fei, H.; Ruan, G.; Xiang, C.; Tour, J. M. Edge-Oriented MoS2 Nanoporous Films as Flexible Electrodes for Hydrogen Evolution Reactions and Supercapacitor Devices. *Adv. Mater.* **2014**, *26*, 8163−8168.

(12) Voiry, D.; Yamaguchi, H.; Li, J.; Silva, R.; Alves, D. C. B.; Fujita, T.; Chen, M.; Asefa, T.; Shenoy, V. B.; Eda, G.; Chhowalla, M. Enhanced catalytic activity in strained chemically exfoliated WS_2 nanosheets for hydrogen evolution. *Nat. Mater.* **2013**, *12*, 850−855.

(13) Georgiou, T.; Jalil, R.; Belle, B. D.; Britnell, L.; Gorbachev, R. V.; Morozov, S. V.; Kim, Y.-J.; Gholinia, A.; Haigh, S. J.; Makarovsky, O.; Eaves, L.; Ponomarenko, L. A.; Geim, A. K.; Novoselov, K. S.; Mishchenko, A. Vertical field-effect transistor based on graphene-WS_2 heterostructures for flexible and transparent electronics. *Nat. Nanotechnol.* **2013**, *8*, 100−103.

(14) Ratha, S.; Rout, C. S. Supercapacitor Electrodes Based on Layered Tungsten Disulfide-Reduced Graphene Oxide Hybrids Synthesized by a Facile Hydrothermal Method. *ACS Appl. Mater. Interfaces* **2013**, *5*, 11427−11433.

(15) Bhandavat, R.; David, L.; Singh, G. Synthesis of Surface-Functionalized WS_2 Nanosheets and Performance as Li-Ion Battery Anodes. *J. Phys. Chem. Lett.* **2012**, *3*, 1523−1530.

(16) Yuan, H. T.; Toh, M.; Morimoto, K.; Tan, W.; Wei, F.; Shimotani, H.; Kloc, C.; Iwasa, Y. Liquid-gated electric-double-layer transistor on layered metal dichalcogenide, SnS_2. *Appl. Phys. Lett.* **2011**, *98*, 012102.

(17) Bai, Y.; Zong, X.; Yu, H.; Chen, Z.-G.; Wang, L. Scalable Low-Cost SnS_2 Nanosheets as Counter Electrode Building Blocks for Dye-Sensitized Solar Cells. *Chem. - Eur. J.* **2014**, *20*, 8670−8676.

(18) Lee, M.-J.; Ahn, J.-H.; Sung, J. H.; Heo, H.; Jeon, S. G.; Lee, W.; Song, J. Y.; Hong, K.-H.; Choi, B.; Lee, S.-H.; Jo, M.-H. Thermoelectric materials by using two-dimensional materials with negative correlation between electrical and thermal conductivity. *Nat. Commun.* **2016**, *7*, 12011.

(19) Kannan, P. K.; Rout, C. S. High Performance Non-enzymatic Glucose Sensor Based on One-Step Electrodeposited Nickel Sulfide. *Chem. - Eur. J.* **2015**, *21*, 9355−9359.

(20) Chou, S.-W.; Lin, J.-Y. Cathodic Deposition of Flaky Nickel Sulfide Nanostructure as an Electroactive Material for High-Performance Supercapacitors. *J. Electrochem. Soc.* **2013**, *160*, D178−D182.

(21) Rakhi, R. B.; Alhebshi, N. A.; Anjum, D. H.; Alshareef, H. N. Nanostructured cobalt sulfide-on-fiber with tunable morphology as electrodes for asymmetric hybrid supercapacitors. *J. Mater. Chem. A* **2014**, *2*, 16190−16198.

(22) Lin, C.-Y.; Mersch, D.; Jefferson, D. A.; Reisner, E. Cobalt sulphide microtube array as cathode in photoelectrochemical water splitting with photoanodes. *Chemical Science* **2014**, *5*, 4906−4913.

(23) Vadivel Murugan, A.; Quintin, M.; Delville, M.-H.; Campet, G.; Vijayamohanan, K. Entrapment of poly(3,4-ethylenedioxythiophene) between VS_2 layers to form a new organic-inorganic intercalative nanocomposite. *J. Mater. Chem.* **2005**, *15*, 902−909.

(24) Feng, J.; Sun, X.; Wu, C.; Peng, L.; Lin, C.; Hu, S.; Yang, J.; Xie, Y. Metallic Few-Layered VS_2 Ultrathin Nanosheets: High Two-Dimensional Conductivity for In-Plane Supercapacitors. *J. Am. Chem. Soc.* **2011**, *133*, 17832−17838.

(25) Therese, H. A.; Rocker, F.; Reiber, A.; Li, J.; Stepputat, M.; Glasser, G.; Kolb, U.; Tremel, W. VS_2 Nanotubes Containing Organic-Amine Templates from the NT-VO_x Precursors and Reversible Copper Intercalation in NT-VS_2. *Angew. Chem., Int. Ed.* **2005**, *44*, 262−265.

(26) Yuan, J.; Wu, J.; Hardy, W. J.; Loya, P.; Lou, M.; Yang, Y.; Najmaei, S.; Jiang, M.; Qin, F.; Keyshar, K.; Ji, H.; Gao, W.; Bao, J.; Kono, J.; Natelson, D.; Ajayan, P. M.; Lou, J. Facile Synthesis of Single Crystal Vanadium Disulfide Nanosheets by Chemical Vapor Deposition for Efficient Hydrogen Evolution Reaction. *Adv. Mater.* **2015**, *27*, 5605−5609.

(27) Ma, Y.; Dai, Y.; Guo, M.; Niu, C.; Zhu, Y.; Huang, B. Evidence of the Existence of Magnetism in Pristine VX_2 Monolayers (X = S, Se) and Their Strain-Induced Tunable Magnetic Properties. *ACS Nano* **2012**, *6*, 1695−1701.

(28) Feng, J.; Peng, L.; Wu, C.; Sun, X.; Hu, S.; Lin, C.; Dai, J.; Yang, J.; Xie, Y. Giant Moisture Responsiveness of VS_2 Ultrathin Nanosheets for Novel Touchless Positioning Interface. *Adv. Mater.* **2012**, *24*, 1969−1974.

(29) Puthussery, J.; Seefeld, S.; Berry, N.; Gibbs, M.; Law, M. Colloidal Iron Pyrite (FeS_2) Nanocrystal Inks for Thin-Film Photovoltaics. *J. Am. Chem. Soc.* **2011**, *133*, 716−719.

(30) Morrish, R.; Silverstein, R.; Wolden, C. A. Synthesis of Stoichiometric FeS_2 through Plasma-Assisted Sulfurization of Fe_2O_3 Nanorods. *J. Am. Chem. Soc.* **2012**, *134*, 17854−17857.

DOI: 10.1021/acs.chemmater.6b05084
Chem. Mater. 2017, 29, 2864−2873

(31) Yersak, T. A.; Macpherson, H. A.; Kim, S. C.; Le, V.-D.; Kang, C. S.; Son, S.-B.; Kim, Y.-H.; Trevey, J. E.; Oh, K. H.; Stoldt, C.; Lee, S.-H. Solid State Enabled Reversible Four Electron Storage. *Adv. Energy Mater.* **2013**, *3*, 120−127.
(32) Jirkovský, J. S.; Björling, A.; Ahlberg, E. Reduction of Oxygen on Dispersed Nanocrystalline CoS_2. *J. Phys. Chem. C* **2012**, *116*, 24436−24444.
(33) Wang, Q.; Jiao, L.; Han, Y.; Du, H.; Peng, W.; Huan, Q.; Song, D.; Si, Y.; Wang, Y.; Yuan, H. CoS_2 Hollow Spheres: Fabrication and Their Application in Lithium-Ion Batteries. *J. Phys. Chem. C* **2011**, *115*, 8300−8304.
(34) Yang, S.-L.; Yao, H.-B.; Gao, M.-R.; Yu, S.-H. Monodisperse cubic pyrite NiS_2 dodecahedrons and microspheres synthesized by a solvothermal process in a mixed solvent: thermal stability and magnetic properties. *CrystEngComm* **2009**, *11*, 1383−1390.
(35) Takeuchi, T.; Sakaebe, H.; Kageyama, H.; Sakai, T.; Tatsumi, K. Preparation of NiS_2 Using Spark-Plasma-Sintering Process and Its Electrochemical Properties. *J. Electrochem. Soc.* **2008**, *155*, A679−A684.
(36) Hillebrand, W. F. The Vanadium Sulphide, Patronite, and its Mineral Associates from Minasragra, Peru. *J. Am. Chem. Soc.* **1907**, *29*, 1019−1029.
(37) Allmann, R.; Baumann, I.; Kutoglu, A.; Rösch, H.; Hellner, E. Die Kristallstruktur des Patronits $V(S_2)_2$. *Naturwissenschaften* **1964**, *51*, 263−264.
(38) Kozlova, M. N.; Mironov, Y. V.; Grayfer, E. D.; Smolentsev, A. I.; Zaikovskii, V. I.; Nebogatikova, N. A.; Podlipskaya, T. Y.; Fedorov, V. E. Synthesis, Crystal Structure, and Colloidal Dispersions of Vanadium Tetrasulfide (VS_4). *Chem. - Eur. J.* **2015**, *21*, 4639−4645.
(39) Rout, C. S.; Kim, B.-H.; Xu, X.; Yang, J.; Jeong, H. Y.; Odkhuu, D.; Park, N.; Cho, J.; Shin, H. S. Synthesis and Characterization of Patronite Form of Vanadium Sulfide on Graphitic Layer. *J. Am. Chem. Soc.* **2013**, *135*, 8720−8725.
(40) Britto, S.; Leskes, M.; Hua, X.; Hébert, C.-A.; Shin, H. S.; Clarke, S.; Borkiewicz, O.; Chapman, K. W.; Seshadri, R.; Cho, J.; Grey, C. P. Multiple Redox Modes in the Reversible Lithiation of High-Capacity, Peierls-Distorted Vanadium Sulfide. *J. Am. Chem. Soc.* **2015**, *137*, 8499−8508.
(41) Zhou, Y.; Li, Y.; Yang, J.; Tian, J.; Xu, H.; Yang, J.; Fan, W. Conductive Polymer-Coated VS_4 Submicrospheres As Advanced Electrode Materials in Lithium-Ion Batteries. *ACS Appl. Mater. Interfaces* **2016**, *8*, 18797−18805.
(42) Sun, R.; Wei, Q.; Li, Q.; Luo, W.; An, Q.; Sheng, J.; Wang, D.; Chen, W.; Mai, L. Vanadium Sulfide on Reduced Graphene Oxide Layer as a Promising Anode for Sodium Ion Battery. *ACS Appl. Mater. Interfaces* **2015**, *7*, 20902−20908.
(43) Ratha, S.; Marri, S. R.; Behera, J. N.; Rout, C. S. High-Energy-Density Supercapacitors Based on Patronite/Single-Walled Carbon Nanotubes/Reduced Graphene Oxide Hybrids. *Eur. J. Inorg. Chem.* **2016**, *2016*, 259−265.
(44) Lui, G.; Jiang, G.; Duan, A.; Broughton, J.; Zhang, J.; Fowler, M. W.; Yu, A. Synthesis and Characterization of Template-Free VS_4 Nanostructured Materials with Potential Application in Photocatalysis. *Ind. Eng. Chem. Res.* **2015**, *54*, 2682−2689.
(45) Guo, W.; Wu, D. Facile synthesis of VS_4/graphene nanocomposites and their visible-light-driven photocatalytic water splitting activities. *Int. J. Hydrogen Energy* **2014**, *39*, 16832−16840.
(46) Hibble, S. J.; Walton, R. I.; Pickup, D. M. Local structures of the amorphous chromium sulfide, CrS_3, and selenide, $CrSe_3$, from X-ray absorption studies. *J. Chem. Soc., Dalton Trans.* **1996**, 2245−2251.
(47) Puurunen, R. L. Surface chemistry of atomic layer deposition: A case study for the trimethylaluminum/water process. *J. Appl. Phys.* **2005**, *97*, 121301.
(48) Dasgupta, N. P.; Meng, X.; Elam, J. W.; Martinson, A. B. F. Atomic Layer Deposition of Metal Sulfide Materials. *Acc. Chem. Res.* **2015**, *48*, 341−348.
(49) Miikkulainen, V.; Leskelä, M.; Ritala, M.; Puurunen, R. L. Crystallinity of inorganic films grown by atomic layer deposition: Overview and general trends. *J. Appl. Phys.* **2013**, *113*, 021301.
(50) Martinson, A. B. F.; Elam, J. W.; Pellin, M. J. Atomic layer deposition of Cu_2S for future application in photovoltaics. *Appl. Phys. Lett.* **2009**, *94*, 123107.
(51) Ham, G.; Shin, S.; Park, J.; Choi, H.; Kim, J.; Lee, Y.-A.; Seo, H.; Jeon, H. Tuning the Electronic Structure of Tin Sulfides Grown by Atomic Layer Deposition. *ACS Appl. Mater. Interfaces* **2013**, *5*, 8889−8896.
(52) McCarthy, R. F.; Weimer, M. S.; Haasch, R. T.; Schaller, R. D.; Hock, A. S.; Martinson, A. B. F. $V_xIn_{(2-x)}S_3$ Intermediate Band Absorbers Deposited by Atomic Layer Deposition. *Chem. Mater.* **2016**, *28*, 2033−2040.
(53) Dasgupta, N. P.; Mack, J. F.; Langston, M. C.; Bousetta, A.; Prinz, F. B. Design of an atomic layer deposition reactor for hydrogen sulfide compatibility. *Rev. Sci. Instrum.* **2010**, *81*, 044102.
(54) Riha, S. C.; Libera, J. A.; Elam, J. W.; Martinson, A. B. F. Design and implementation of an integral wall-mounted quartz crystal microbalance for atomic layer deposition. *Rev. Sci. Instrum.* **2012**, *83*, 094101.
(55) Nelson, A. Co-refinement of multiple-contrast neutron/X-ray reflectivity data using MOTOFIT. *J. Appl. Crystallogr.* **2006**, *39*, 273−276.
(56) Hohenberg, P.; Kohn, W. Inhomogeneous Electron Gas. *Phys. Rev.* **1964**, *136*, B864−B871.
(57) Kresse, G.; Hafner, J. *Ab initio* molecular-dynamics simulation of the liquid-metal-amorphous-semiconductor transition in germanium. *Phys. Rev. B: Condens. Matter Mater. Phys.* **1994**, *49*, 14251−14269.
(58) Kresse, G.; Furthmüller, J. Efficient iterative schemes for *ab initio* total-energy calculations using a plane-wave basis set. *Phys. Rev. B: Condens. Matter Mater. Phys.* **1996**, *54*, 11169−11186.
(59) Perdew, J. P.; Burke, K.; Ernzerhof, M. Generalized Gradient Approximation Made Simple. *Phys. Rev. Lett.* **1996**, *77*, 3865−3868.
(60) Porezag, D.; Pederson, M. R. Infrared intensities and Raman-scattering activities within density-functional theory. *Phys. Rev. B: Condens. Matter Mater. Phys.* **1996**, *54*, 7830−7836.
(61) Fonari, A.; Stauffer, S. vasp_raman.py; 2013; https://github.com/raman-sc/VASP/.
(62) Meng, X.; Libera, J. A.; Fister, T. T.; Zhou, H.; Hedlund, J. K.; Fenter, P.; Elam, J. W. Atomic Layer Deposition of Gallium Sulfide Films Using Hexakis(dimethylamido)digallium and Hydrogen Sulfide. *Chem. Mater.* **2014**, *26*, 1029−1039.
(63) McCarthy, R. F.; Weimer, M. S.; Emery, J. D.; Hock, A. S.; Martinson, A. B. F. Oxygen-Free Atomic Layer Deposition of Indium Sulfide. *ACS Appl. Mater. Interfaces* **2014**, *6*, 12137−12145.
(64) Reverberi, A. P.; Klemeš, J. J.; Varbanov, P. S.; Fabiano, B. A review on hydrogen production from hydrogen sulphide by chemical and photochemical methods. *J. Cleaner Prod.* **2016**, *136*, 72.
(65) Powder Diffraction File (PDF 00-021-1434). In *The International Centre for Diffraction Data*; International Centre for Diffraction Data: Newtown Square, PA, 1964.
(66) Powder Diffraction File (PDF 00-019-1407). In *The International Centre for Diffraction Data*; International Centre for Diffraction Data: Newtown Square, PA, 1965.
(67) Ishii, M.; Wada, H.; Nozaki, H.; Kawada, I. Raman studies of $(Fe, V)_3S_4$ solid solution. *Solid State Commun.* **1982**, *42*, 605−608.
(68) Baddour-Hadjean, R.; Pereira-Ramos, J. P.; Navone, C.; Smirnov, M. Raman Microspectrometry Study of Electrochemical Lithium Intercalation into Sputtered Crystalline V_2O_5 Thin Films. *Chem. Mater.* **2008**, *20*, 1916−1923.
(69) Coyle, G. J.; Tsang, T.; Adler, I.; Yin, L. XPS studies of ion-bombardment damage of transition metal sulfides. *J. Electron Spectrosc. Relat. Phenom.* **1980**, *20*, 169−182.
(70) Kasperkiewicz, J.; Kovacich, J. A.; Lichtman, D. XPS studies of vanadium and vanadium oxides. *J. Electron Spectrosc. Relat. Phenom.* **1983**, *32*, 123−132.
(71) Tsang, T.; Coyle, G. J.; Adler, I.; Yin, Y. XPS studies of ion bombardment damage of iron−sulfur compounds. *J. Electron Spectrosc. Relat. Phenom.* **1979**, *16*, 389−396.

DOI: 10.1021/acs.chemmater.6b05084
Chem. Mater. 2017, 29, 2864−2873

(72) Sangaletti, L.; Parmigiani, F.; Thio, T.; Bennett, J. W. Electronic-correlation effects in the x-ray-photoemission spectra of NiS_2. *Phys. Rev. B: Condens. Matter Mater. Phys.* **1997**, *55*, 9514−9519.
(73) Leiro, J. A.; Mattila, S. S.; Laajalehto, K. XPS study of the sulphur 2p spectra of pyrite. *Surf. Sci.* **2003**, *547*, 157−161.
(74) Hamdadou, N.; Khelil, A.; Bernède, J. C. Pyrite FeS_2 films obtained by sulphuration of iron pre-deposited films. *Mater. Chem. Phys.* **2003**, *78*, 591−601.
(75) Yokoyama, M.; Yoshimura, M.; Wakihara, M.; Somiya, S.; Taniguchi, M. Synthesis of vanadium sulfides under high pressure. *J. Solid State Chem.* **1985**, *60*, 182−187.

DOI: 10.1021/acs.chemmater.6b05084
Chem. Mater. 2017, 29, 2864−2873